Inorganic Chemistry
Article

Inorg. Chem. **2010**, *49*, 6535–6544 **6535**
DOI: 10.1021/ic100362q

Spectroscopic and Computational Studies of a Series of High-Spin Ni(II) Thiolate Complexes

Katherine M. Van Heuvelen,[†] Jaeheung Cho,[‡,§] Timothy Dingee,[†] Charles G. Riordan,[‡] and Thomas C. Brunold*[,†]

[†]*Department of Chemistry, University of Wisconsin-Madison, Madison, Wisconsin 53706, and*
[‡]*Department of Chemistry and Biochemistry, University of Delaware, Newark, Delaware 19716.*
[§]*Present address: Department of Chemistry and Nano Science, Ewha Womans University, Seoul 120-750, Korea*

Received February 22, 2010

The electronic structures of a series of high-spin Ni(II)-thiolate complexes of the form [PhTt^{tBu}]Ni(SR) (R = CPh_3, **2**; C_6F_5, **3**; C_6H_5, **4**; PhTt^{tBu} = phenyltris((*tert*-butylthio)methyl)borate) have been characterized using a combined spectroscopic and computational approach. Resonance Raman (rR) spectroscopic data reveal that the ν_{Ni-SR} vibrational feature occurs between 404 and 436 cm^{-1} in these species. The corresponding rR excitation profiles display a striking de-enhancement behavior because of interference effects involving energetically proximate electronic excited states. These data were analyzed in the framework of time-dependent Heller theory to obtain quantitative insight into excited state nuclear distortions. The electronic absorption and magnetic circular dichroism spectra of **2**−**4** are characterized by numerous charge transfer (CT) transitions. The dominant absorption feature, which occurs at ∼18,000 cm^{-1} in all three complexes, is assigned as a thiolate-to-Ni CT transition involving molecular orbitals that are of π-symmetry with respect to the Ni−S bond, reminiscent of the characteristic absorption feature of blue copper proteins. Density functional theory computational data provide molecular orbital descriptions for **2**−**4** and allow for detailed assignments of the key spectral features. A comparison of the results obtained in this study to those reported for similar Ni-thiolate species reveals that the supporting ligand plays a secondary role in determining the spectroscopic properties, as the electronic structure is primarily determined by the metal−thiolate bonding interaction.

1. Introduction

While only a relatively small number of nickel metalloenzymes are known, acetyl-coenzyme A synthase/carbon monoxide dehydrogenase (ACS/CODH),[1] [NiFe] hydrogenase,[2−4] and Ni superoxide dismutase (NiSOD)[5,6] each contain Ni−S(cysteine) bonds at their active sites. Ni−thiolate bonds may also be formed in the catalytic cycle of methyl-coenzyme M reductase, though this has not yet been definitively established.[7] Active site thiolate moieties appear to play a crucial role in tuning the redox potentials and, thus, controlling the reactivity of these metalloenzymes.[8] The nature of Ni−thiolate bonding interactions has been investigated primarily through the preparation and characterization of synthetic compounds. Examples of such synthetic Ni(II)-thiolate species include the five-coordinate complexes [Ni(tmc)SR]OTf (tmc = 1,4,8,11-tetramethyl-1,4,8,11-tetraazacyclotetradecane, R = C_6H_5, C_2H_5)[9] and [L^8py_2Ni(S−C_6H_4-*p*-CH_3)]BPh_4 (L^8py_2 = 1,5-bis(2-pyridylmethyl)-1,5-diazacyclooctane),[10] pseudotetrahedral species of the form $PhB(CH_2PPh_2)_3NiX$ (X = I, Cl, N_3, OR, SR),[11] and LNi (L = *R,R′-N,N′*-bis(1-carboxy-2-mercaptoethyl)-1,2-diaminoethane or *N,N′*-bis(2-methyl-2-mercaptoprop-1-yl)-1,3-diamino-2,2-dimethylpropane), which resembles the distal nickel site of ACS/CODH.[12]

*To whom correspondence should be addressed. E-mail: brunold@chem.wisc.edu.

(1) Darnault, C.; Volbeda, A.; Kim, E. J.; Legrand, P.; Vernede, X.; Lindahl, P. A.; Fontecilla-Camps, J. C. *Nat. Struct. Biol.* **2003**, *10*, 271–279.
(2) Higuchi, Y.; Yagi, T.; Yasuoka, N. *Structure* **1997**, *5*, 1671–1680.
(3) Volbeda, A.; Charon, M. H.; Piras, C.; Hatchikian, E. C.; Frey, M.; Fontecilla-Camps, J. C. *Nature* **1995**, *373*, 580–587.
(4) Volbeda, A.; Garcin, E.; Piras, C.; de Lacey, A. L.; Fernandez, V. M.; Hatchikian, E. C.; Frey, M.; Fontecilla-Camps, J. C. *J. Am. Chem. Soc.* **1996**, *118*, 12989–12996.
(5) Barondeau, D. P.; Kassmann, C. J.; Bruns, C. K.; Tainer, J. A.; Getzoff, E. D. *Biochemistry* **2004**, *43*, 8038–8047.
(6) Wuerges, J.; Lee, J. W.; Yim, Y. I.; Yim, H. S.; Kang, S. O.; Carugo, K. D. *Proc. Nat. Acad. Sci. U.S.A.* **2004**, *101*, 8569–8574.
(7) Harmer, J.; Finazzo, C.; Piskorski, R.; Ebner, S.; Duin, E. C.; Goenrich, M.; Thauer, R. K.; Reiher, M.; Schweiger, A.; Hinderberger, D.; Jaun, B. *J. Am. Chem. Soc.* **2008**, *130*, 10907–10920.
(8) Maroney, M. J. *Curr. Opin. Chem. Biol.* **1999**, *3*, 188–199.
(9) Ram, M. S.; Riordan, C. G.; Ostrander, R.; Rheingold, A. L. *Inorg. Chem.* **1995**, *34*, 5884–5892.
(10) Fox, D. C.; Fiedler, A. T.; Halfen, H. L.; Brunold, T. C.; Halfen, J. A. *J. Am. Chem. Soc.* **2004**, *126*, 7627–7638.
(11) MacBeth, C. E.; Thomas, J. C.; Betley, T. A.; Peters, J. C. *Inorg. Chem.* **2004**, *43*, 4645–4662.
(12) Stibrany, R. T.; Fox, S.; Bharadwaj, P. K.; Schugar, H. J.; Potenza, J. A. *Inorg. Chem.* **2005**, *44*, 8234–8242.

Published on Web 06/21/2010

A major difficulty in preparing synthetic active-site models involves enforcing the coordination environments observed in biological systems. Steric constraints in a protein, such as those imposed by the polypeptide backbone and amino-acid residues adjacent to the active site, can force metal centers to adopt unexpected geometries. For example, the metal center in plastocyanin and other blue copper proteins adopts a distorted tetrahedral geometry instead of the square planar coordination commonly observed for four-coordinate Cu(II) complexes.[13,14] The presence of both thiolate and thioether ligation of the Cu ion in blue copper proteins (originating from cysteine and methionine residues, respectively) poses an additional challenge in the preparation of synthetic model compounds. Tuning the steric and electronic properties of the supporting ligand is instrumental in overcoming these difficulties. Notably, synthetic compounds that mimic the structural and spectroscopic properties of plastocyanin have recently been reported, such as a Cu(II) species with a ligand set containing both a thioether and a thiolate.[15]

Recently, the Okamoto group reported the synthesis of a series of metal−thiolate complexes of the form [Tp^{iPr2}]-MSC_6F_5 (Tp^{iPr2} = hydrotris(3,5-diisopropyl-1-pyrazolyl)-borate; M = Mn, Fe, Co, Ni (**1**), Cu, Zn), with the copper-containing species serving as a model for plastocyanin.[16] The tripodal supporting ligand imposes a four-coordinate, distorted tetrahedral geometry and stabilizes the M(II) oxidation state. Intense S(thiolate)→M(II) charge transfer transitions dominate the electronic absorption (Abs) spectra of these complexes, and the covalency of the M−thiolate bond increases with the increasing effective nuclear charge of the metal from Mn(II) to Cu(II).[17,18]

A four-coordinate, distorted tetrahedral geometry similar to that observed for [Tp^{iPr2}]MSC_6F_5 can also be enforced by the tripodal thioether supporting ligand $PhTt^{tBu}$ (phenyltris((*tert*-butylthio)methyl)borate). The presence of bulky substituents (here tBu) leaves an empty coordination site that can be occupied by a wide range of ligands, such as halides ([$PhTt^{tBu}$]NiCl),[19] carbon monoxide ([$PhTt^{tBu}$]NiCO),[20] or thiolates ([$PhTt^{tBu}$]NiSR).[21] The $PhTt^{tBu}$ ligand has also been shown to allow for the formation of nickel dimers with bridging ligands from the oxygen group, namely, [{($PhTt^{tBu}$)-Ni}$_2$(μ-O)$_2$] and [{($PhTt^{tBu}$)Ni}$_2$(μ-η^2:η^2-S_2)].[22−25] Notably, the use of a methyl group in place of the bulky *tert*-butyl moiety leads to the formation of six-coordinate monomers of the form [PhTt]$_2$M (M = Fe, Co, Ni).[26]

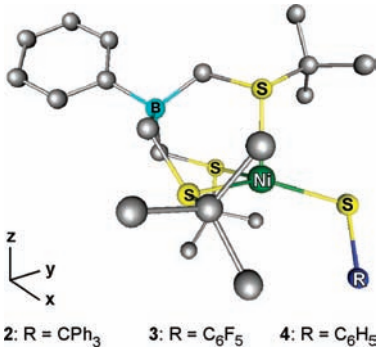

Figure 1. Structures of compounds **2**, **3**, and **4**. H atoms are omitted for clarity. Note that the Ni−S(thiolate) bond vector roughly bisects the **x**- and **y**-axes of the molecular coordinate system shown in the bottom left corner.

Recently, some of us reported the preparation and preliminary spectroscopic characterization of a series of four-coordinate, high-spin Ni(II)-thiolate species, [$PhTt^{tBu}$]Ni(SR) (R = CPh_3, **2**; C_6F_5, **3**; C_6H_5, **4**) (Figure 1).[21] All of these species contain the same thioether supporting ligand but differ with respect to the electron-withdrawing ability of the R group, thus allowing for a detailed analysis of the Ni−S-(thiolate) bonding interaction and its dependence on the nature of R. In the present study we have employed Abs, magnetic circular dichroism (MCD), and resonance Raman (rR) spectroscopies in conjunction with density functional theory (DFT) and time-dependent DFT (TD-DFT) computational methods to investigate the electronic structures of these Ni-thiolate complexes.

2. Experimental Section

A. Spectroscopy. Compounds **2**−**4** were synthesized according to a previous report,[21] and samples suitable for low temperature studies were prepared in 1:1 solutions of $CHCl_3$/toluene (**2**, 0.7 mM; **3**, 1.0 mM; **4**, 1.2 mM). Room temperature Abs spectra were collected on a spectrophotometer (Hewlett-Packard 8453) equipped with a circulating water bath. Low temperature Abs and MCD spectra of **2**−**4** were obtained using a spectropolarimeter (Jasco J-715) in conjunction with a magnetocryostat (Oxford Instruments SM-4000 8T). To eliminate contributions from glass strain to the MCD data, the −7 T spectrum was subtracted from the +7 T spectrum.

For rR studies, samples of **2**−**4** in $CHCl_3$ (**2**, 10 mM; **3**, 5 mM; **4**, 5 mM) were prepared in NMR tubes. An Ar^+ ion laser (Coherent I-305), a Kr^+ ion laser (Coherent I-302C), and a dye laser (Coherent 599−01, equipped with rhodamine 6G dye) pumped by the Ar^+ laser were used as the excitation sources, maintaining a power of 20−30 mW at the sample. Samples were placed in an EPR dewar filled with liquid nitrogen to minimize photodecomposition. The scattered light was collected at a ∼135° backscattering angle from the surface of the sample and dispersed by a triple monochromator (Acton Research) with 1200 or 2400 grooves/mm gratings. Data were accumulated using a CCD camera (Princeton Instruments Spec X: 100 BR deep depletion, back-thinned, 1340 × 100 pixels). The 669 and 370 cm^{-1} peaks of the $CHCl_3$ solvent were used as internal

(13) Holm, R. H.; Kennepohl, P.; Solomon, E. I. *Chem. Rev.* **1996**, *96*, 2239–2314.
(14) Solomon, E. I.; Szilagyi, R. K.; DeBeer George, S.; Basumallick, L. *Chem. Rev.* **2004**, *104*, 419–458.
(15) Holland, P. L.; Tolman, W. B. *J. Am. Chem. Soc.* **2000**, *122*, 6331–6332.
(16) Matsunaga, Y.; Fujisawa, K.; Ibi, N.; Miyashita, Y.; Okamoto, K.-i. *Inorg. Chem.* **2005**, *44*, 325–335.
(17) Gorelsky, S. I.; Basumallick, L.; Vura-Weis, J.; Sarangi, R.; Hodgson, K. O.; Hedman, B.; Fujisawa, K.; Solomon, E. I. *Inorg. Chem.* **2005**, *44*, 4947–4960.
(18) Chattopadhyay, S.; Deb, T.; Ma, H.; Petersen, J. L.; Young, V. G.; Jensen, M, P. *Inorg. Chem.* **2008**, *47*, 3384–3392.
(19) Schebler, P. J.; Riordan, C. G.; Guzei, I. A.; Rheingold, A. L. *Inorg. Chem.* **1998**, *37*, 4754–4755.
(20) Craft, J. L.; Mandimutsira, B. S.; Fujita, K.; Riordan, C. G.; Brunold, T. C. *Inorg. Chem.* **2003**, *42*, 859–867.
(21) Cho, J.; Yap, G. P. A.; Riordan, C. G. *Inorg. Chem.* **2007**, *46*, 11308–11315.
(22) Cho, J.; Van Heuvelen, K. M.; Yap, G. P. A.; Brunold, T. C.; Riordan, C. G. *Inorg. Chem.* **2008**, *47*, 3931–3933.
(23) Schenker, R.; Mandimutsira, B. S.; Riordan, C. G.; Brunold, T. *J. Am. Chem. Soc.* **2002**, *124*, 13842–13855.
(24) Van Heuvelen, K. M.; Cho, J.; Riordan, C. G.; Brunold, T. C. *Inorg. Chem.* **2010**, *49*, 3113–3120.
(25) Mandimutsira, B. S.; Yamarik, J. L.; Brunold, T. C.; Gu, W.; Cramer, S. P.; Riordan, C. G. *J. Am. Chem. Soc.* **2001**, *123*, 9194–9195.
(26) Ohrenberg, C.; Ge, P. H.; Schebler, P.; Riordan, C. G.; Yap, G. P. A.; Rheingold, A. L. *Inorg. Chem.* **1996**, *35*, 749–754.

standards for calibrating the frequencies and intensities, respectively, of the rR features of **2**−**4**.

B. Electronic Structure Calculations. B.1. Geometry Optimizations. All density functional theory (DFT) geometry optimizations were performed on a cluster of Intel Xeon processors (ACE computers) using the Amsterdam Density Functional (ADF) 2006 suite of programs.[27−30] For all atoms, the ADF basis set IV (a triple-ζ basis set) was employed and core orbitals were frozen through 1s for C, N, and O, and through 2p for Ni and S. The integration constant was set to 5.0, and the Vosko−Wilk−Nusair local density approximation (VWN-LDA)[31] was used along with the nonlocal gradient corrections of Becke for exchange[32] and Perdew for correlation.[33] Initial models for geometry optimization studies were derived from the X-ray crystal structures of **2**−**4** and included the complete structure of each species.[21] The SCF convergence criterion was set at 1×10^{-5} hartrees, and the geometry was considered converged when the maximum gradient fell below 0.0065 hartree/Å.

B.2. Single Point and Time-Dependent DFT Calculations. The ORCA 2.6.35 software package developed by Dr. Frank Neese[34] was used to perform single point DFT and time-dependent DFT (TD-DFT) calculations on models of **2**−**4**. For each complex, the energy-minimized structure obtained from geometry optimization studies was truncated by replacing the *tert*-butyl and phenyl moieties of the $PhTt^{tBu}$ supporting ligand with methyl groups. Becke's three-parameter hybrid functional for exchange[35,36] and the Lee−Yang−Parr functional for correlation[37] (B3LYP/G) were used with the polarized split valence (SV(P)) basis[38] and the SV/C auxiliary basis[39] for all atoms except Ni and S, for which Ahlrichs' polarized triple-ζ valence polarization (TZVP)[38] and double-ζ valence polarization (DZP)[40] basis sets were employed, respectively. Fifty excited states were considered in all TD-DFT calculations.

The results from TD-DFT calculations were used to simulate Abs spectra by assuming that each electronic transition gives rise to a Gaussian band with a full width at half-maximum corresponding to that determined via Gaussian deconvolution of the experimental Abs and MCD data (**2**, $\nu_{1/2}$ = 1,680 cm^{-1}; **3**, $\nu_{1/2}$ = 2,110 cm^{-1}; **4**, $\nu_{1/2}$ = 1,850 cm^{-1}). In each case the calculated Abs intensity was scaled by a factor of 4 to facilitate a direct comparison with the experimental spectra. Isosurface plots of key molecular orbitals (MOs) and electron density difference maps (EDDMs) were generated with the gOpenMol program developed by Laaksonen[41] using isodensity values of 0.03 au and 0.003 au, respectively.

C. Abs and rR Excitation Profile Data Simulations. The relevant portions of the 4 K Abs spectrum and 77 K rR excitation profiles of **4** were simulated using time-dependent Heller theory[42,43] as implemented in a MathCAD script.[44] A damping factor of $\Gamma = 500\ cm^{-1}$ was used for all three excited states considered.

3. Results and Analysis

A. Spectroscopy. A.1. Abs and MCD. Previous studies revealed that the room temperature electronic absorption (Abs) spectrum of **3** is dominated by a broad feature in the visible region (ν_{max} = 19,610 cm^{-1}, ε = 4,800 M^{-1} cm^{-1}) that was assigned as a ligand-to-metal charge transfer (LMCT) transition. The Abs spectra of **2** and **4** are qualitatively similar, each displaying a broad feature that is red-shifted relative to that of **3** by ∼800 cm^{-1} and ∼2,000 cm^{-1}, respectively (**2**, ν_{max} = 18,800 cm^{-1}, ε = 7,500 M^{-1} cm^{-1}; **4**, ν_{max} = 17,575 cm^{-1}, ε = 4,100 M^{-1} cm^{-1}).[21] This trend in relative Abs energies was rationalized previously in terms of the different electronic properties of the thiolate substituent R. Specifically, it was proposed that an increase in the electron-withdrawing ability of the R group stabilizes the thiolate S 3p-based orbitals and therefore increases ν_{max}.[21]

Upon changing the solvent from $CHCl_3$ to a 1:1 mixture of $CHCl_3$:toluene and lowering the temperature to 4 K, the dominant Abs feature of each species undergoes a blue-shift of ∼250 cm^{-1} and displays a slight apparent decrease in intensity (**2**, ν_{max} = 19,050 cm^{-1}, ε = 7,375 M^{-1} cm^{-1}; **3**, ν_{max} = 19,920 cm^{-1}, ε = 4,360 M^{-1} cm^{-1}; **4**, ν_{max} = 17,840 cm^{-1}, ε = 3,020 M^{-1} cm^{-1}) (Figure 2). Importantly, however, the trends in both the relative energies (**3** > **2** > **4**) and intensities (**2** > **3** > **4**) of the dominant Abs feature observed at higher temperature are preserved at 4 K. Lowering the temperature also causes a significant sharpening of the Abs features, leading to the appearance of fine structure not observable at 298 K.

To obtain further insight into the electronic structures of **2**−**4**, magnetic circular dichroism (MCD) spectroscopy was used. In each case the MCD signal intensities displayed the temperature-dependent *C*-term behavior characteristic of high-spin Ni(II) species (data not shown), consistent with previously reported NMR and magnetic susceptibility data.[21] The MCD spectra of all three complexes (Figure 2) exhibit a derivative-shaped feature at ∼19,000 cm^{-1} that can be attributed to a pseudo-*A* term derived from overlapping, oppositely signed *C*-terms based on its temperature dependence. To determine the number of electronic transitions contributing to the 4 K Abs and MCD spectra of each Ni-thiolate species, the spectra were subjected to simultaneous Gaussian deconvolutions. This analysis revealed that a minimum of seven electronic transitions occur between 9,000 and 33,300 cm^{-1} for **2** and **3**, while an eighth Gaussian band was necessary to properly reproduce the Abs and MCD spectra of **4**. The relative Abs and MCD intensities of the individual features suggest that the spectra of all three species are dominated by LMCT transitions above ∼12,500 cm^{-1}, while the lower-energy features are attributable to Ni d→d transitions. In support of these band assignments, the Ni d→d transitions of pseudotetrahedral Ni(II) species containing sulfur ligands typically occur between 6,500 and 12,500 cm^{-1}.[16,45] More detailed spectral assignments are provided in section 3.B.3.

(27) Baerends, E. J.; Ellis, D. E.; Ros, P. *Chem. Phys.* **1973**, *2*, 41.
(28) Guerra, C. F.; Snijders, J. G.; te Velde, G.; Baerends, E. J. *Theor. Chem. Acc.* **1998**, *99*, 391–403.
(29) Velde, G. T.; Baerends, E. J. *J. Comput. Phys.* **1992**, *99*, 84–98.
(30) Versluis, L.; Ziegler, T. *J. Chem. Phys.* **1988**, *88*, 322–328.
(31) Vosko, S. H.; Wilk, L.; Nusair, M. *Can. J. Phys.* **1980**, *58*, 1200–1211.
(32) Becke, A. D. *J. Chem. Phys.* **1986**, *84*, 4524–4529.
(33) Perdew, J. P. *Phys. Rev. B* **1986**, *33*, 8822–8824.
(34) Neese, F. *ORCA 2.6.35, an ab initio, density functional, and semi-empirical program package*; Max-Planck-Institut für Bioanorganische Chemie: Mülheim an der Ruhr, Germany, 2008.
(35) Becke, A. D. *J. Chem. Phys.* **1993**, *98*, 5648–5652.
(36) Becke, A. D. *J. Chem. Phys.* **1993**, *98*, 1372–1377.
(37) Lee, C. T.; Yang, W. T.; Parr, R. G. *Phys. Rev. B* **1988**, *37*, 785–789.
(38) Schafer, A.; Horn, H.; Ahlrichs, R. *J. Chem. Phys.* **1992**, *97*, 2571–2577.
(39) Weigend, F.; Haser, M. *Theor. Chem. Acc.* **1997**, *97*, 331–340.
(40) The Ahlrichs DZ basis set was obtained from the TurboMole basis set library under ftp.chemi.unikarlsruhe.de/pub/basen.
(41) Laaksonen, L. *J. Mol. Graphics* **1992**, *10*, 33–34.
(42) Bailey, S. E.; Cohan, J. S.; Zink, J. I. *J. Phys. Chem. B* **2000**, *104*, 10743–10749.
(43) Kim Shin, K. S.; Zink, J. I. *J. Am. Chem. Soc.* **1990**, *112*, 7148–7157.
(44) *MathCAD, Professional 2001i*; MathSoft Engineering & Education, Inc.: Cambridge, MA, 2001.

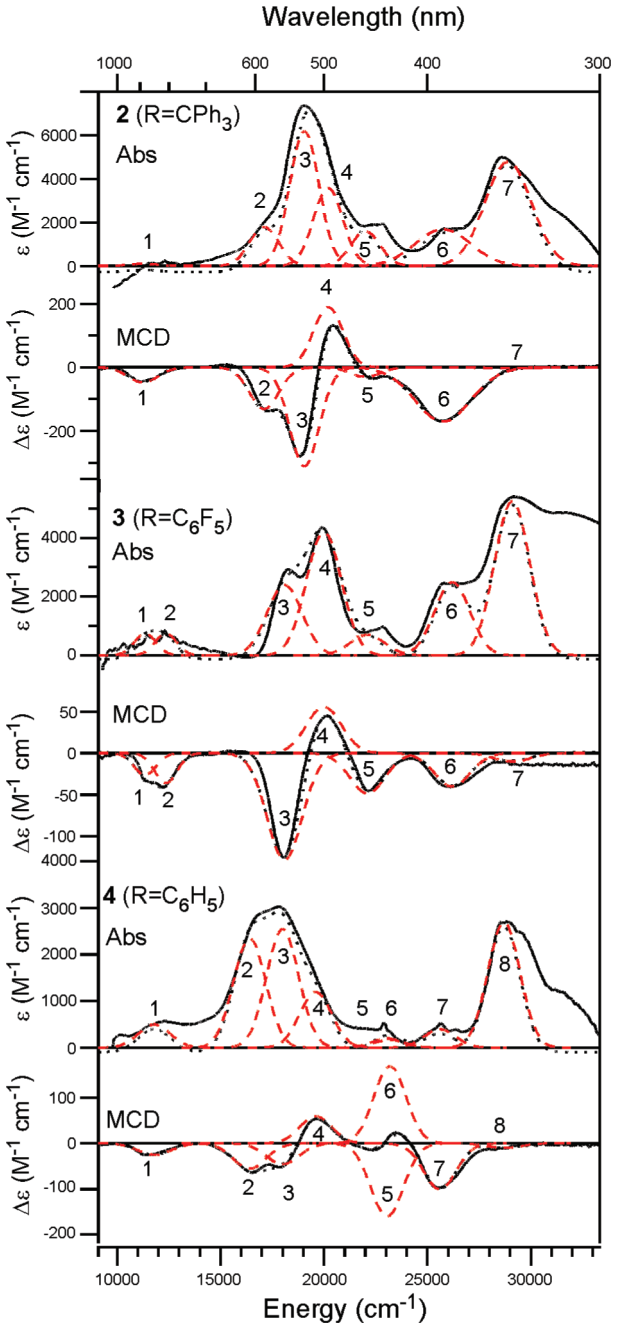

Figure 2. Abs and 7 T MCD spectra collected at 4 K of **2** (top), **3** (middle), and **4** (bottom), along with the individual Gaussian bands (dashed lines) and their sums (dotted lines) as obtained from combined fits of these data sets. The fit parameters are summarized in Table 1.

A.2. Resonance Raman. The resonance Raman (rR) spectrum of **2** obtained with 531 nm laser excitation (Figure 3, top) is characterized by an intense peak at 415 cm^{-1} that is assigned as the Ni−S(thiolate) stretching mode, ν_{Ni-SR}, based on its energy and observed enhancement behavior (vide infra); the first overtone of this feature is apparent at 820 cm^{-1}. As shown in Figure 3, similar vibrational features are observed in the rR spectra of **3** (ν_{Ni-SR} = 404 cm^{-1}) and **4** (ν_{Ni-SR} = 436 cm^{-1}, $2\nu_{Ni-SR}$ = 871 cm^{-1}). For comparison, the analogous

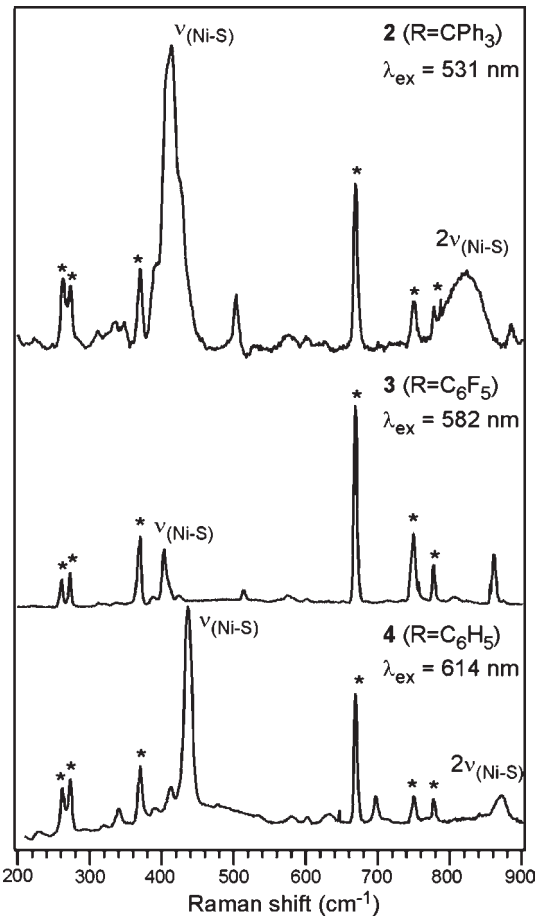

Figure 3. 77 K rR spectra of **2** (top), **3** (middle), and **4** (bottom). $CHCl_3$ solvent peaks are marked with an asterisk.

Ni−S(thiolate) stretch of **1**, which contains the same -SC_6F_5 moiety as **3**, was observed at 410 cm^{-1}.[17] In addition to the intense ν_{Ni-SR} band, the rR spectra of **2**−**4** exhibit several weakly enhanced features at 312, 338, 388, 412, and 424 cm^{-1}. Our previous investigations of $[\{(PhTt^{tBu})Ni(II)\}_2(\mu\text{-}\eta^2\text{:}\eta^2\text{-}S_2)]$ revealed Ni−S(thioether) vibrational modes at 289, 348, and 411 cm^{-1}.[23,24] This comparison suggests that many of the weakly enhanced features apparent in the rR spectra of **2**−**4** arise from Ni−S(thioether) vibrations involving the $PhTt^{tBu}$ supporting ligand.

The ν_{Ni-SR} features in the rR spectra of **3** and **4** are significantly sharper than the 415 cm^{-1} band of **2**, which contains both low- and high-energy shoulders. To this end, it is interesting to note that two distinct conformers of **2** were observed by X-ray crystallography, termed **2α** and **2*β*** (the latter, observed at a higher resolution than **2α**, served as the basis for our computational studies described below).[21] Small differences in Ni−S(thiolate) bond lengths and Ni−S−C angles between the two conformations would likely cause the energies of the corresponding ν_{Ni-SR} modes to differ slightly. However, rR spectra of **2** collected at 273 K, where a rapid interconversion between different conformations should occur, show a similarly broad, asymmetric ν_{Ni-SR} feature (see Supporting Information, Figure S3). Therefore, the 415 cm^{-1} rR feature of **2** is presumably a composite of several overlapping bands associated with the Ni−S(thiolate)

(45) Lever, A. B. P. *Inorganic Electronic Spectroscopy*, 2nd ed.; Elsevier Science Publishing Co., Inc.: New York, 1984.

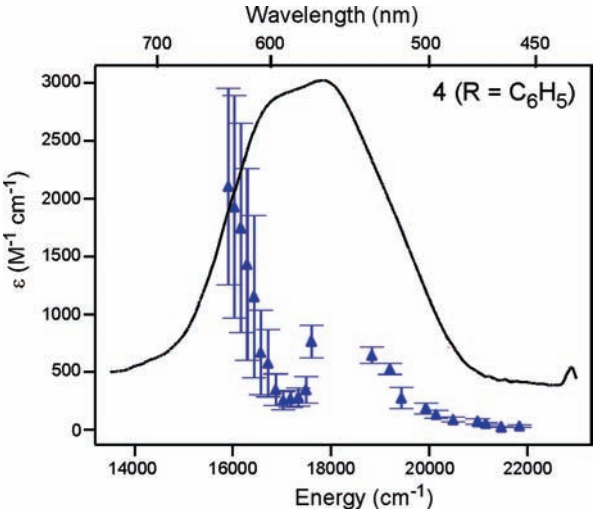

Figure 4. rR excitation profile of the ν_{Ni-SR} vibrational mode (▲) along with the 4 K Abs spectrum (solid line) of **4**.

stretch and multiple Ni−S(thioether) vibrations that occur in this region.

The rR excitation profile for the ν_{Ni-SR} = 436 cm^{-1} vibrational feature of **4** is shown in Figure 4. Surprisingly, the shape of this excitation profile deviates significantly from the Abs envelope. Typically, maximum rR enhancement is observed when λ_{ex} coincides with the Abs peak position (λ_{max}) such that the excitation profile roughly mirrors the Abs spectrum. However, in the case of **4**, the intensity of ν_{Ni-SR} displays preresonance enhancement and then falls off sharply as λ_{ex} approaches λ_{max}. The low laser power and short scan times employed during the rR data collection suggest that this peculiar behavior does not originate from sample decomposition. Additionally, the use of an internal standard, namely, the solvent band at 370 cm^{-1}, in close energetic proximity to the 436 cm^{-1} vibrational feature and the low concentration (5 mM) of the sample ensured that reabsorption did not distort the excitation profile. Instead, the rR excitation profile behavior of **4** is characteristic of a de-enhancement phenomenon resulting from destructive interference between the Raman scattering cross sections associated with energetically proximate electronic excited states.[42,43] Qualitatively similar, though somewhat less dramatic, de-enhancement behavior was observed for **2** and **3** (Supporting Information, Figures S1 and S2); therefore, only the results obtained for **4** were examined in detail (see Section 3.C).

B. Computations. B.1. Geometry Optimizations. DFT geometry optimizations were conducted using initial atomic coordinates derived from the X-ray crystal structures of **2**−**4**.[21] As shown in Table 2, the agreement between experimental and DFT-optimized bond lengths and angles is excellent. Importantly, the degree of distortion from ideal tetrahedral geometry observed crystallographically, as expressed in terms of the pyramidalization parameter τ (as defined in Table 2, with τ = 0 and τ = 1 describing tetrahedral and trigonal pyramidal limiting geometries),[46] is accurately reproduced in the optimized models.

B.2. DFT-Computed Bonding Descriptions. Quantitative bonding descriptions for **2**−**4** were generated by carrying out spin-unrestricted DFT calculations with the three-parameter B3LYP/G hybrid functional. Atomic coordinates used for these single point calculations were derived from the geometry-optimized models, and the supporting ligand was truncated for computational practicality as described in section 2.B.2.

To interpret the computed molecular orbital (MO) diagrams for **2**−**4**, it is useful to consider first the thiolate (SR) fragment orbitals participating in metal−ligand bonding.[47] The highest-energy MOs of the SR fragments of **4** (Figure 5, top) and **3** are derived from the two sulfur 3p orbitals that are oriented perpendicular to the S−C bond vector. These orbitals are referred to as π(ip) and π(op) based on their orientation with respect to the plane of the aromatic ring, where ip and op stand for in-plane and out-of-plane, respectively. The nature of the bonding interactions between the SR fragment orbitals and the Ni 3d orbitals is determined by the Ni−S−R bond angle and the pyramidalization parameter τ. The Ni−S−R angles of 110−122° and relatively large values of τ (0.69−0.9) for **2**−**4** (Table 2) are indicative of a distorted trigonal pyramidal geometry. Consequently, the SR π(op) fragment orbital is perpendicular with respect to the Ni−SR bond vector and interacts with the Ni 3d(x^2-y^2) orbital in a π fashion, as illustrated by the highest occupied molecular orbital (HOMO) of **4** in Figure 6. In contrast, the SR π(ip) fragment orbital is oriented roughly parallel to the Ni−SR bond and thus forms a σ bond with the Ni 3d(xy) orbital (Figure 6). Comparable Ni−S π and σ interactions also occur in **2** and **3**; however, in the case of **2** the delocalization of electron density over the SR moiety is different than in **3** and **4**, as the sulfur atom is not directly bound to an aromatic ring (Figure 5, bottom). The implications of this difference are discussed below.

Isosurface plots of the relevant spin-down (β) MOs of **2** and **4** are plotted in Figure 6, and the compositions of the frontier orbitals for all three complexes investigated are listed in Table 3. In each case, the lowest-energy unoccupied molecular orbital (LUMO) is derived primarily from the Ni 3d(x^2-y^2) orbital, which is π-antibonding with the SR π(op) fragment MO and σ-antibonding with the thioether supporting ligand. The Ni 3d(z^2)-derived MO (LUMO+1) is destabilized relative to the LUMO because it is strongly σ-antibonding with respect to the Ni−thioether bonds. The highest-energy occupied MO (HOMO) is composed primarily of the SR π(op) orbital, which is π-bonding with the Ni 3d(x^2-y^2) orbital. The HOMO-1, which has predominant SR π(ip) orbital character, is stabilized relative to the HOMO because it is σ-bonding with respect to the Ni−SR bond. Toward lower energy, MOs primarily derived from the thioether supporting ligand separate the thiolate-based HOMO and HOMO-1 from the occupied Ni 3d(xy, xz, yz)-based MOs, which are significantly stabilized relative to the unoccupied Ni 3d(x^2-y^2, z^2) MOs.

B.3. TD-DFT Results and Spectral Assignments. The TD-DFT computed Abs spectra for truncated models of **2**−**4** (section 3.B.2.) along with the corresponding

(46) Vela, J.; Stoian, S.; Flaschenriem, C. J.; Munck, E.; Holland, P. L. *J. Am. Chem. Soc.* **2004**, *126*, 4522–4523.

(47) The MOs described herein are derived from a Löwdin population analysis.

Table 1. Fit Parameters Obtained from Gaussian Deconvolutions of the 4 K Abs and MCD Spectra of **2**, **3**, and **4** (Figure *2*)

band	ν_{max} (cm^{-1})	$\nu_{1/2}$ (cm^{-1})	ε_{max} (M^{-1} cm^{-1})	osc. strength ($f_{ex} \times 10^3$)[a]	$\Delta\varepsilon$ (M^{-1} cm^{-1})
			2 (R = CPh_3)		
1	11250	1680	100	0.8	−47
2	17100	1680	1800	13.9	−130
3	19050	1680	6200	48.0	−310
4	20200	1680	3600	27.9	190
5	22000	1680	1600	12.4	−30
6	25750	3192	1700	25.0	−170
7	28900	2591	4800	57.3	−3
			3 (R = C_6F_5)		
1	11350	1260	750	4.4	−26
2	12350	1260	750	4.4	−36
3	18100	2016	2400	22.3	−128
4	20000	2016	4200	39.0	56
5	22100	2016	700	6.5	−48
6	26200	2016	2500	23.2	−40
7	29100	2016	5250	48.8	−10
			4 (R = C_6H_5)		
1	11800	1848	500	4.3	−25
2	16400	1848	2350	20.0	−55
3	18000	1848	2550	21.7	−45
4	19600	1848	1200	10.2	60
5	23050	1848	200	1.7	−160
6	23190	1848	170	1.5	170
7	25600	1848	400	3.4	−100
8	28700	1848	2700	23.0	−10

[a] Oscillator strength, $f_{ex} = (4.61 \times 10^{-9})\ \varepsilon_{max}\nu_{1/2}$.

Table 2. Experimental and Calculated Structural Parameters for **2**−**4**

	2 (R = CPh_3)		**3** (R = C_6F_5)		**4** (R = C_6H_5)	
	Exp.	Calc.	Exp.	Calc.	Exp.	Calc.
Ni−SR (Å)	2.184	2.196	2.235	2.238	2.186	2.210
Ni−S($PhTt^{tBu}$) (Å)	2.312	2.358	2.329	2.314	2.295	2.313
	2.294	2.302	2.284	2.290	2.300	2.284
	2.347	2.332	2.292	2.336	2.285	2.319
Ni−S−R	122.0°	124.2°	110.5°	113.2°	111.6°	113.4°
τ[a]	0.90	0.82	0.74	0.74	0.69	0.69

[a] $\tau = [\sum\angle (L_{basal}-M-L_{basal}) - \sum\angle (L_{axial}-M-L_{basal})]/90°$, see ref 46.

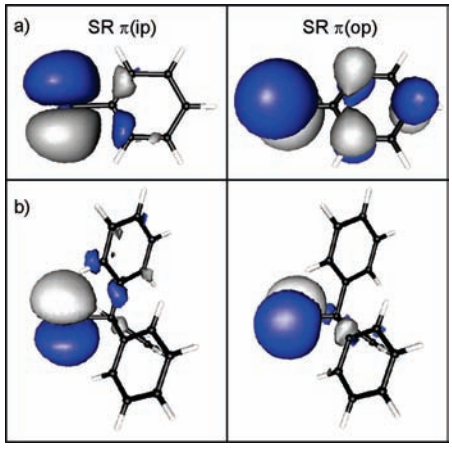

Figure 5. Isosurface plots of the highest-energy occupied MOs of the SR fragments of **4** (top) and **2** (bottom). Note that the π(ip) and π(op) nomenclature is somewhat arbitrary in the case of **2**.

experimental spectra are shown in Figure 7. Importantly, TD-DFT properly reproduces the trend in relative peak positions of the dominant Abs features of **2**−**4** observed experimentally, thus warranting a more detailed analysis of the computational results.

The experimental Abs spectrum of **4** is dominated by a broad feature at 17,840 cm^{-1} that was initially assigned as a LMCT transition; this feature is well-reproduced in the TD-DFT calculated spectrum (note that the higher energy of the calculated band relative to its experimental counterpart reflects the tendency of TD-DFT to overestimate the energies of electronic transitions[48,49]). An analysis of the electron density difference map (EDDM) associated with this transition reveals that electron density is transferred primarily from the SR π(op) HOMO to the Ni 3d(x^2-y^2)-derived LUMO (Figure 7, panels b and c). This assignment is consistent with the predominant enhancement of the ν_{Ni-SR} vibrational mode in the rR spectrum of **4** obtained with laser excitation in this region (Figure 3). The TD-DFT computed Abs spectrum also permits the assignment of the weak, low-energy feature observed experimentally (band 1 in Table 1) as a ligand-field transition and identifies the donor and acceptor orbitals as the Ni 3d($xz + yz$)- and Ni 3d(x^2-y^2)-based MOs, respectively (Figure 7, panel a). Because of the close energetic proximity of the SR and S(thioether) frontier orbitals, the features between ~25,000 and 30,000 cm^{-1} arise from LMCT transitions involving both the $PhTt^{tBu}$ supporting ligand and the SR moiety. Computations predict that intraligand electronic transitions dominate the Abs spectrum above ~30,000 cm^{-1} (Figure 7, panel e).

(48) Craft, J. L.; Horng, Y. C.; Ragsdale, S. W.; Brunold, T. C. *J. Biol. Inorg. Chem.* **2004**, *9*, 77–89.
(49) Schenker, R.; Kieber-Emmons, M. T.; Riordan, C. G.; Brunold, T. C. *Inorg. Chem.* **2005**, *44*, 1752–1762.

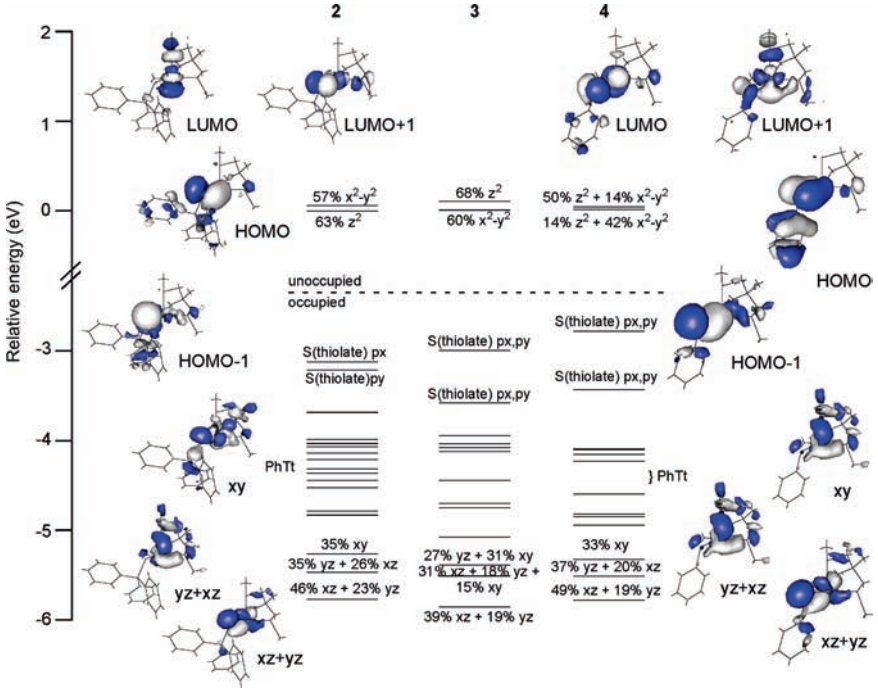

Figure 6. Partial MO energy diagrams for **2**, **3**, and **4** obtained from spin-unrestricted DFT calculations, along with isosurface plots of the key MOs for **2** and **4**. Only the spin-down (β) MOs are shown, and their energies are given relative to that of the corresponding LUMO. The relevant MOs are labeled according to their primary contributors.

Table 3. Energies (in eV) and Compositions (%) of the Relevant Ni 3d- and SR π-Based Spin-down (β) MOs (see Figure 6 for MO plots)

E (eV)	MO[a]	occ.[b]	Ni	S(thiolate)	R	PhTt^{tBu}
			2 (R = CPh_3)			
−2.62	Ni 3d (LUMO+1)	0	57 x^2-y^2, 2 z^2	20	3	18
−2.68	Ni 3d (LUMO)	0	63 z^2, 5 xy	1	2	29
−5.79	SR π(op) (HOMO)	1	7 x^2-y^2	52	15	26
−5.89	SR π(ip) (HOMO-1)	1	4 xz, 4 xy	54	12	26
			3 (R = C_6F_5)			
−2.95	Ni 3d (LUMO+1)	0	68 z^2, 3 yz	1	1	27
−3.05	Ni 3d (LUMO)	0	60 x^2-y^2, 1 z^2	11	6	22
−6.05	SR π(op) (HOMO)	1	5 x^2-y^2	46	30	19
−6.63	SR π(ip) (HOMO-1)	1	6 xz, 9 xy	47	3	35
			4 (R = C_6H_5)			
−2.68	Ni 3d (LUMO+1)	0	50 z^2, 14 x^2-y^2	5	5	26
−2.71	Ni 3d (LUMO)	0	42 x^2-y^2, 14 z^2	12	6	26
−5.50	SR π(op) (HOMO)	1	10 x^2-y^2	41	34	15
−6.16	SR π(ip) (HOMO-1)	1	7 xz, 2 yz, 8 xy	53	4	26

[a] Principal orbital contributor. [b] Occupancy of corresponding MO.

The TD-DFT results for **2** and **3** indicate that similar electronic transitions occur in all three complexes (Figure 7), consistent with the experimental Abs spectra (Figure 2). The reduced admixture of S(thiolate) orbital character to the Ni 3d($xz + yz$)-based MO in **2** and **3** relative to **4** leads to a decreased stabilization of this orbital and, thus, a decrease in the calculated energy and intensity of the low-energy ligand field transition, which is nicely verified experimentally by the blue-shift of band 1 from **2** and **3** to **4** (Table 1).

C. rR Excitation Profile Analysis. The peculiar rR excitation profile of the ν_{Ni-SR} mode obtained for **4** (Figure 4) was analyzed using time-dependent (TD) Heller theory to gain insight into the origin of this apparent de-enhancement behavior. In general, the intensity of a vibrational feature in a rR spectrum (I_{rR}) is proportional to the square of the Raman scattering cross section (α), $I_{rR} \propto \alpha^2$, resulting in resonance enhancement behavior in which the excitation profile roughly mirrors the Abs spectrum in that region. However, if multiple excited states exist in close energetic proximity, which is the case for complexes **2**−**4**, the Raman intensity becomes proportional to the square of the *sum* of the scattering cross sections, $I_{rR} \propto [\sum\alpha]^2$.[50−53]

(50) Heller, E. J.; Sundberg, R. L.; Tannor, D. *J. Phys. Chem.* **1982**, *86*, 1822–1833.
(51) Lee, S.-Y.; Heller, E. J. *J. Chem. Phys.* **1979**, *71*, 4777–4788.
(52) Tannor, D. J.; Heller, E. J. *J. Chem. Phys.* **1982**, *77*, 202–218.

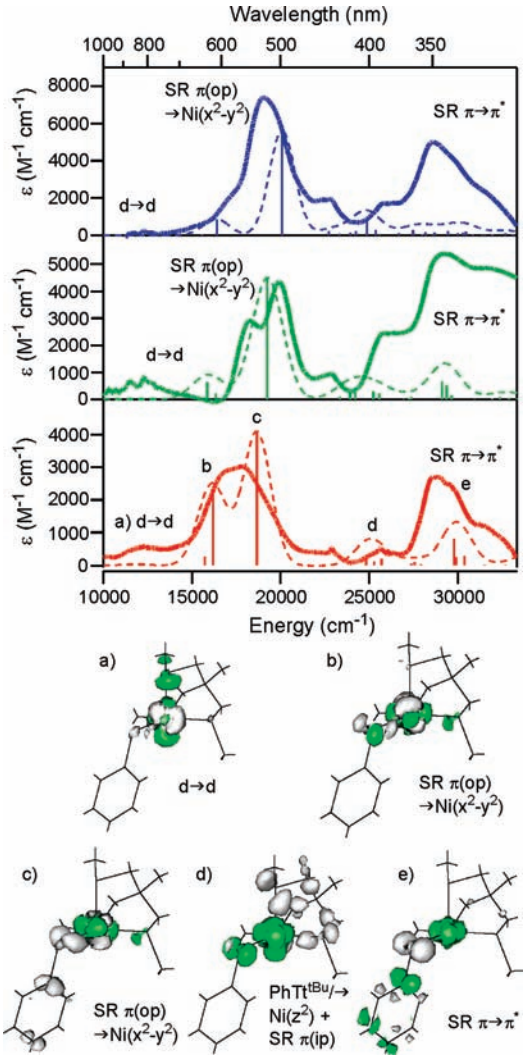

Figure 7. Top: TD-DFT-predicted (dashed line) and experimental 4 K (solid line) Abs spectra of **2** (top), **3** (middle), and **4** (bottom). The calculated intensities were scaled by a factor of 1/4 to facilitate a direct comparison with the experimental spectra. Bottom: Electron density difference maps (EDDMs) showing the loss and gain of electron density (gray and green, respectively) for select transitions of **4**.

As a result, an unexpected loss of rR intensity can occur because of constructive and destructive interference between the cross sections associated with different excited states. Such interference effects can lead to de-enhancement behavior, as observed in the case of **4**.

To analyze the 4 K Abs and 77 K rR excitation profile data of **4** using TD Heller theory,[42,43] we considered the excited states associated with bands 2−4 (Table 1, Figure 2) and included the Ni−S(thiolate) vibrational band, ν_{Ni-SR}, at 436 cm^{-1} and the Ni−S(thioether) vibrational band at 411 cm^{-1}. The zero-phonon transition energies, E_{0n}, of the three excited states were estimated from the Gaussian-resolved experimental Abs spectrum and the value of the dimensionless displacement of each state, n, in relation to the ground state along mode k, ($\Delta_{n,k}$) was systematically varied to achieve the best

(53) Zink, J. I.; Kim Shin, K.-S. Molecular Distortions in Excited Electronic States Determined From Electronic and Resonance Raman Spectroscopy. In *Advances in Photochemistry*; Volman, D. H., Hammond, G. S., Neckers, D. C., Eds.; Wiley: New York, 1991; Vol. *16*.

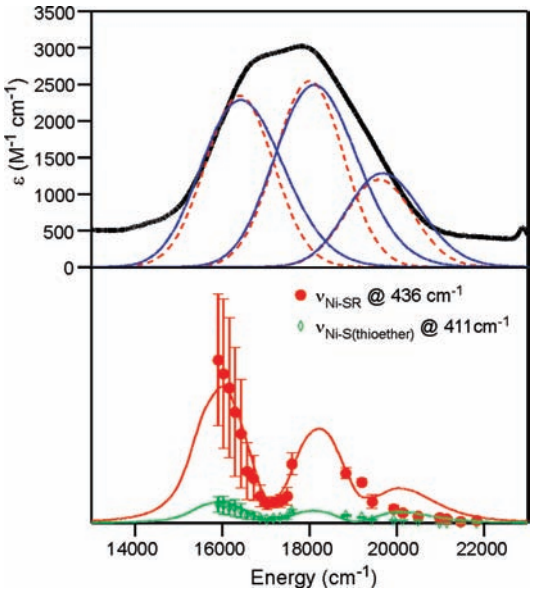

Figure 8. Top: Experimental 4 K Abs spectrum of **4** (thick solid line), Gaussian bands 2−4 from Figure 2 (dashed lines), and TD Heller simulated individual Abs bands (thin solid lines) obtained using the parameters listed in Table 4. Bottom: Corresponding experimental rR excitation profiles for the 436 and 411 cm^{-1} modes (red circles and green diamonds, respectively) along with the simulated rR excitation profiles (red and green solid lines, respectively).

Table 4. Excited-State Parameters Determined by Simultaneous Fitting of the Abs and rR Excitation Profile Data of **4** Using TD Heller Theory

parameter	state 1	state 2	state 3
E_{0n} (cm^{-1})[a]	15,100	17,050	18,950
Δ_{411}	0.8	0.8	1.0
Δ_{436}	1.9	1.9	1.3

[a] E_{0n} is the energy of the zero-phonon transition between the ground state and excited state n.

simultaneous fit of the experimental Abs and rR excitation profile data (Figure 8). The optimized parameters from this analysis are presented in Table 4.

Using the parameters obtained from the TD Heller analysis of the Abs and rR excitation profile data of **4** (Table 4), the Ni−SR bond length in the excited states corresponding to Gaussian bands 2 and 3 can be estimated by treating the Ni−SR unit as a diatomic harmonic oscillator with effective masses of 58.7 and 109 g/mol for Ni and the SR moiety, respectively. This is a reasonable assumption considering that the SR moiety of **3** is 90 g/mol heavier than that of **4**, which should lower ν_{Ni-SR} from 436 cm^{-1} in **4** to 400 cm^{-1} in **3** (exp. ν_{Ni-SR} = 404 cm^{-1} in **3**). The Ni−PhTt^{tBu} moiety was also treated as a diatomic harmonic oscillator with effective masses of 58.69 and 397.60 g/mol, respectively. The general formula to convert the dimensionless displacement parameters listed in Table 4 to the nuclear distortions in each excited state is given in eq 1.[53]

$$\delta = \sqrt{\frac{6.023 \times 10^{23}}{\mu} \times \frac{\hbar}{2\pi c\omega}} \times 10^{8} \times \Delta \qquad (1)$$

Here, μ is the effective reduced mass associated with the vibrational mode considered, ω is the energy of the

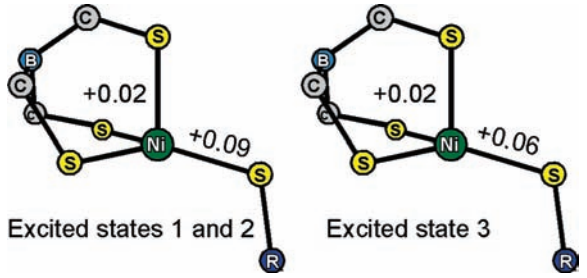

Figure 9. Experimentally derived nuclear distortions of **4** in the first, second, and third excited states corresponding to Gaussian bands 2, 3, and 4 in Figures 2 and 8.

vibrational mode in cm^{-1}, and c is the speed of light in $cm \cdot s^{-1}$. To estimate the magnitude of the Ni−S-(thioether) bond length change in each excited state, $\delta_{n,411}$ was divided by $\sqrt{3}$, since $\delta_{n,411} = 1/\sqrt{3} \cdot (\Delta r_1 + \Delta r_2 + \Delta r_3)$ and $\Delta r_1 = \Delta r_2 = \Delta r_3$ (hence, $\Delta r = \delta_{n,411}/\sqrt{3}$). The results of the excited state distortion analysis are summarized in Figure 9. Note that because the first and second excited states have the same Δ values (i.e., $\Delta_{1,k} \equiv \Delta_{2,k}$) the nuclear distortions in these excited states are identical. The ∼0.09 Å elongation of the Ni−SR bond in the first and second excited states is consistent with the TD-DFT-derived assignment of the dominant Abs feature as a thiolate-to-Ni charge transfer transition (vide supra); excitation into this feature transfers electron density from the Ni−SR π-bonding SR π(op)-based MO to the π-antibonding Ni 3d(x^2-y^2)-based spin-down LUMO (Figure 6). This reduces the overall bond order, which weakens and, thus, lengthens the Ni−SR bond (Figure 9). The DFT-computed bonding description for **4** predicts negligible contributions to these MOs from the thioether supporting ligand, a finding that is corroborated by the minimal molecular distortions along the Ni−S(thioether) bonds in excited states 1 and 2. Analogous to the first and second excited states, the major distortion in the third excited state occurs along the Ni−SR bond (Figure 9).

4. Discussion

A. Influence of Thiolate Substituent on Electronic Properties. The structural and electronic properties of the thiolate substituent (R) strongly modulate the Ni−SR bonding interactions and, thus, the observed spectroscopic properties of **2**−**4**. The relative intensities of the dominant Abs feature that arises from thiolate-to-Ni charge transfer transitions (**2** > **3** > **4**) clearly reflect the different electronic properties of the R groups. In compounds **3** and **4**, the sulfur is directly bound to an aryl group. Significant π interactions between the S 3p atomic orbitals and the frontier orbitals of the aromatic ring result in the delocalization of electron density onto the R moiety, thereby causing a decrease in the intensity of the dominant Abs feature. In contrast, the sulfur atom of the SR ligand of **2** is bound to an sp^3-hybridized carbon atom. As a result, electron density remains more localized in the S 3p orbitals, and **2** exhibits the most intense thiolate-to-Ni charge transfer transition in this series of compounds. While differences in the structural parameter τ may also exert a small influence on the relative intensities of the observed Abs features (an ideal trigonal pyramidal geometry would improve the Ni−SR orbital overlap and thus increase the observed molar absorptivity),[21] the DFT calculations presented herein suggest that the relative intensities of the LMCT bands in these complexes are largely determined by the electronic properties of the thiolate substituent.

On the basis of mass considerations alone, **2** with its heavy thiolate SR group should exhibit the lowest ν_{Ni-SR} frequency, followed by **3** and then **4**. However, our rR data indicate that ν_{Ni-SR} of **3** occurs at a lower frequency than that of **2**, consistent with the fact that the crystallographically determined Ni−SR bond length in **3** is longer than in **2** and **4**. This finding indicates that several factors affect the Ni−SR stretching frequency. In fact, in addition to the reduced mass and bond strength, mechanical coupling between nuclear motions may also influence the frequencies of vibrational modes.[54] The broadening of the 415 cm^{-1} vibrational band observed in the rR spectrum of **2** reveals that considerable mixing of Ni−S-(thioether) and Ni−SR stretching motions can indeed occur in these compounds.

B. Influence of Supporting Ligand: Thioether versus Pyrazole. The influence of the supporting ligand on the electronic structure of Ni-thiolate compounds can be assessed on the basis of a comparison between **1** and **3**. Both are four-coordinate Ni(II) species that contain a pentafluorophenyl thiolate ligand, differing only with respect to their supporting ligands (tripodal pyrazole and thioether in **1** and **3**, respectively).

Despite this latter difference, the spectroscopic properties of **1** and **3** are qualitatively similar. rR spectroscopic studies revealed that the ν_{Ni-SR} stretching mode of **1** occurs at 410 cm^{-1}, as compared to 404 cm^{-1} for **3**.[17] Likewise, features that arise from ligand-field and charge transfer transitions dominate the Abs and MCD spectra of each compound below and above 13,000 cm^{-1}, respectively.[17] Nonetheless, the intense SR π(op)→Ni 3d(x^2-y^2) transition that dominates the Abs spectrum is blue-shifted considerably in **1** (ν_{max} = 23,200 cm^{-1}, ε = 3,060 $M^{-1}\,cm^{-1}$) versus **3** (ν_{max} = 19,920 cm^{-1}, ε = 4,360 $M^{-1}\,cm^{-1}$). This difference can be understood by noting that the $PhTt^{tBu}$ thioether-based frontier orbitals of **3** are in close energetic proximity to the fragment orbitals derived from the thiolate moiety, thereby destabilizing the SR π(op) and π(ip) orbitals and causing a red-shift of the SR π(op)→Ni transition in **3** relative to **1**.

The spectroscopic similarities between **1** and **3** are also reflected in the DFT-computed electronic structure descriptions for these two compounds. The spin-down LUMO and LUMO+1 have predominantly Ni 3d-(x^2-y^2) and Ni 3d(z^2) orbital character, respectively, while the HOMO and HOMO-1 are derived from the SR π(op) and SR π(ip) fragment orbitals, respectively. The Ni−S(thiolate) bond covalency, as judged from the DFT-computed compositions of the LUMO, is comparable in **1** and **3** (the LUMO of each compound contains 8% and 12% S 3p orbital character, respectively).[17] Collectively, these results demonstrate that, while the substitution of a thioether for a pyrazole supporting ligand slightly stabilizes the SR fragment orbitals and

(54) Brunold, T. C.; Tamura, N.; Kitajima, N.; Moro-oka, Y.; Solomon, E. I. *J. Am. Chem. Soc.* **1998**, *120*, 5674–5690.

causes a red-shift of the dominant LMCT transition, the spectroscopic properties and electronic structures of **1** and **3** are qualitatively very similar.

This finding, namely, that the Ni−thiolate interaction is the principle contributor to the electronic structures of **1** and **3**, agrees with our current understanding of Ni-containing enzymes. Ni−S(cysteine) ligation is a common feature in the active sites of redox-active Ni metalloenzymes,[8] and in the case of NiSOD this highly covalent bonding interaction is thought to tune the Ni(III/II) redox potential such as to provide access to the Ni(III) state in the catalytic cycle.[55,56] The influence of the thiolate ligand on redox potential is evident in the previously reported Ni(II/I) redox couples of **2**−**4**, which vary by ∼140 mV as a function of the electron withdrawing properties of the R group ($E_{1/2}$ = −1.03 V, **3**; −1.11 V, **2**; −1.17 V, **4**, vs Fc(+/0).[21]

5. Conclusions

In this study, we have employed a combination of spectroscopic and computational methods to characterize a series of high-spin Ni(II)-thiolate complexes and obtained significant new insight into the nature of their Ni−S(thiolate) bonding interactions. The rR excitation profile data of **2**−**4** exhibit deenhancement behavior characteristic of interference effects involving multiple electronic excited states, which were analyzed for **4** in the framework of TD Heller theory. The calculated 0.09 Å elongation of the Ni−SR bond in the excited state associated with the dominant Abs feature supports the TD-DFT-based assignment of this feature as a thiolate-to-Ni charge transfer transition. A comparison of the spectroscopic data obtained for **2**−**4** demonstrates that the nature of the thiolate substituent has a profound influence on the electronic properties of Ni(II) thiolate compounds.

Acknowledgment. This work has been supported by the NIH (GM 64631 to T.C.B.), the NSF Graduate Research Fellowship program (K.M.V.H.), and the NSF (CHE-0518508 and CHE-0809603 to C.G.R.). We thank Professor Frank Neese, Universität Bonn, for providing us with a free copy of ORCA.

Supporting Information Available: Atomic coordinates of the geometry-optimized models **2**−**4** (Tables S1−S3), rR excitation profiles of **2** and **3** (Figures S1, S2), rR spectra collected at 77 and 273 K (Figures S3, S4), and frontier MOs of **2** and **3** (Figure S5). This material is available free of charge via the Internet at http://pubs.acs.org.

(55) Choudhury, S. B.; Lee, J.-W.; Davidson, G.; Yim, Y.-I.; Bose, K.; Sharma, M. L.; Kang, S.-O.; Cabelli, D. E.; Maroney, M. J. *Biochemistry* **1999**, *38*, 3744–3752.

(56) Johnson, O. E.; Ryan, K. C.; Maroney, M. J.; Brunold, T. C. *J. Biol. Inorg. Chem.* **2010**, *15*, 777–793.